Ceramics International 49 (2023) 36276–36288

Contents lists available at ScienceDirect

Ceramics International

journal homepage: www.elsevier.com/locate/ceramint

Fabrication and functional characteristics of micro/nano structures on the RB-SiC surface through nanosecond pulsed laser irradiation

Hong An [a], Yongfeng Qian [a,**], Lin Zhang [b], Zhiyu Zhang [c], Hu Huang [a,*], Jiwang Yan [b]

[a] Key Laboratory of CNC Equipment Reliability, Ministry of Education, School of Mechanical and Aerospace Engineering, Electron Microscopy Center, Jilin University, Changchun, 130022, China

[b] Department of Mechanical Engineering, Faculty of Science and Technology, Keio University, Yokohama, 223-8522, Japan

[c] Key Laboratory of Optical System Advanced Manufacturing Technology, Changchun Institute of Optics, Fine Mechanics and Physics, Chinese Academy of Sciences, Changchun, 130033, China

ARTICLE INFO

Handling Editor: Dr P. Vincenzini

Keywords:
Reaction-bonded silicon carbide
Laser irradiation
Micro/nano structures
Superhydrophilicity
Reflectivity

ABSTRACT

Reaction-bonded silicon carbide (RB-SiC) is gaining increasing attention due to its exceptional mechanical properties contributed by the dispersion of hard silicon carbide (SiC) and silicon (Si), which has been extensively applied in aerospace and automobile industries. Fabrication of micro/nano structures on the RB-SiC surface can endow it some specific functional properties, but conventional manufacturing procedures face challenges due to the intrinsic hard-brittle nature of RB-SiC. In the present study, various micro/nano structures, including dome-like particle structures, micro-cone structures and the spider web-like film, are fabricated on the RB-SiC surface by nanosecond pulsed laser irradiation under different experimental conditions. Comparative experiments are performed to explore the effects of laser power and scanning speed on the microscopic morphology and chemical composition. Consequently, the ablation mechanism is clarified. The formation of micro-cone structures covered by the spider web-like film can result in a wettability transition of the RB-SiC surface from hydrophilicity to superhydrophilicity. In addition, by introducing the spider web-like film, the reflectivity of the RB-SiC surface is increased by an impressive 83% or more in the wavelength range of 200 to 2500 nm. This study provides a method for improving the surface properties of RB-SiC substrates using a laser-based approach, which is anticipated to expand their application prospects as functional materials.

1. Introduction

Reaction-bonded silicon carbide (RB-SiC) is a two-phase composite material consisting of silicon carbide (SiC) particles bonded by a silicon (Si) matrix. As an exceptional ceramic material with extremely high strength and hardness, outstanding chemical attack resistance and excellent stability, it has a wide range of applications in the automobile, aerospace, aviation, military and other cutting-edge fields [1–5]. Additionally, benefitting from the unique properties of large band gap, high thermal conductivity, and breakdown voltage, RB-SiC has also been widely used as a semiconductor material for the preparation of high-speed power devices such as high-voltage diodes and thyristors [6–8]. Fabrication of micro/nano structures on the surface of materials can effectively improve its service performance and functional properties [9–12]. Conventional machining methods, such as mechanical machining and chemical etching, have been extensively applied to generate micro/nano structures on the surfaces of various materials. Kong et al. [13] prepared frustum ridge structures and frustum pillar structures on the surface of PMMA using an ultra-precision raster milling technique, which converts an intrinsically hydrophilic surface into a superhydrophobic one. By ultrasonic chemical etching in combination with boiling, hydrangea-like micro/nano structures were fabricated on the aluminum surface, which improved corrosion resistance as well as anti-icing/frosting performance [14]. However, the conventional machining methods mentioned above are not suitable for surface processing of RB-SiC. Because RB-SiC is harder than the majority of machining tool materials, surface damage and tool wear are serious during the machining process [15,16]. Furthermore, the Si and SiC contained in RB-SiC have different physical and chemical properties, making the selection of chemical reagents for the chemical etching

* Corresponding author.
** Corresponding author.
E-mail addresses: qianyf@jlu.edu.cn (Y. Qian), huanghu@jlu.edu.cn (H. Huang).

https://doi.org/10.1016/j.ceramint.2023.08.310
Received 6 August 2023; Received in revised form 24 August 2023; Accepted 28 August 2023
Available online 29 August 2023

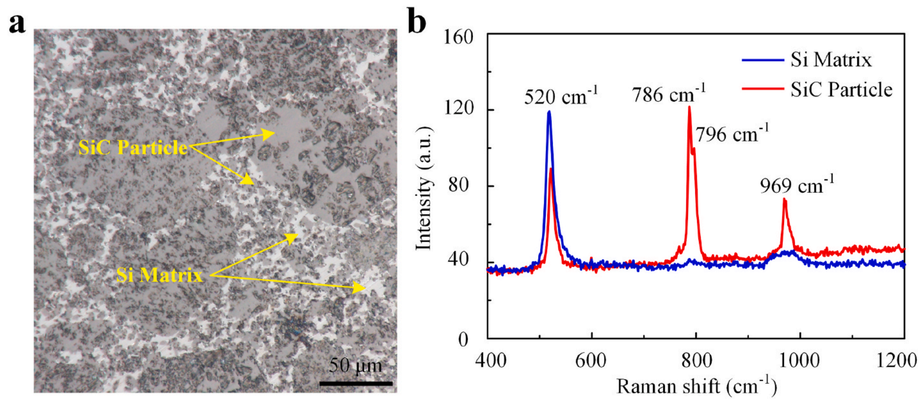

Fig. 1. Surface characterization of the RB-SiC sample: (a) optical micrograph; (b) Raman spectral curves.

process difficult [17].

Based on the aforementioned issues, it is critical to develop a method for manufacturing micro/nano structures on the RB-SiC surface because conventional processing technology is not qualified for high-quality and high-efficient processing [18]. Currently, laser processing technology has gained widespread recognition and utilization owing to its unique advantages such as non-contact processing, no tool wear, and wide adaptability of the machined materials [19,20]. Additionally, laser processing technology also demonstrates the advantages of simplified operation, rapid processing, and environmentally friendly [21,22]. Consequently, laser processing technology is an effective way of dealing with hard-brittle materials [23]. When the applied laser intensity exceeds the ablation threshold of the RB-SiC material, the RB-SiC is removed via vaporization or decomposition, and micro/nano structures can be formed on the surface following condensation deposition [24–26]. For example, Tushar et al. [17] fabricated geometrically aligned cones on the RB-SiC surface by nanosecond pulsed laser irradiation, and the effects of laser irradiation parameters on the surface morphology were investigated. By femtosecond pulsed laser irradiation, laser-induced periodic surface structures (LIPSS) and condensation structures were fabricated on the RB-SiC surface, and a preliminary model was established to describe the ablation and removal mechanism [27]. Although laser irradiation is an effective technique for preparing micro/nano structures on the RB-SiC surface, the ablation process and mechanism are complex because RB-SiC is a two-phase material. In addition, the types of micro/nano structures obtained by laser irradiation of SiC are very limited at present, and their associated functional properties need to be further developed.

In this study, taking advantage of the difference in physical properties of Si matrix and SiC particles contained in RB-SiC, some novel micro/nano structures, including dome-like particle structures, microcone structures, and spider web-like films, were prepared on the surface of RB-SiC by nanosecond pulsed laser irradiation. The microscopic morphologies and chemical compositions of surface micro/nano structures obtained under different laser irradiation conditions were comparatively investigated. In addition, the formation mechanism of various micro/nano structures was discussed. Finally, the influence of the micro/nano structures on the surface wettability behavior and optical properties was studied. This work paves an avenue for understanding the laser-matter interaction and modulation of surface functional properties of RB-SiC.

2. Materials and experiments

The RB-SiC samples used in experiments are cuboid with the size of 20 mm × 20 mm × 5 mm. Before laser irradiation, the samples were magnetorheologically polished to a smooth surface (with a relatively low surface roughness (Sa) of 0.124 μm) to detect the distribution of SiC and Si phases in RB-SiC. Fig. 1(a) shows an optical micrograph of the RB-SiC surface where the SiC particles (gray) and Si matrix (white) can be identified. The majority of large-scale SiC particles do not directly bond, and there are Si and relatively small-scale SiC particles in the interval. The chemical composition of the RB-SiC sample was characterized by a Raman spectroscopy, and the corresponding Raman spectral curves are depicted in Fig. 1(b). The results showed that the Raman peak at around 520 cm^{-1} are observed, which corresponds to the Si phase. While there are two prominent peaks at around 786 and 969 cm^{-1}, both of which correspond to the SiC phase [28].

Table 1
Laser processing parameters.

Laser medium	Value
Wavelength (nm)	1064
Spot size (μm)	43
Power (W)	4.0,7.6,11.2,14.7,18.4,22.0
Scanning speed (mm/s)	10,20,30,40,50,60
Frequency (kHz)	700
Pulse width (ns)	7

The laser irradiation equipment used in this study is a nanosecond pulsed laser (SP-050P-A-EP-Z-F-Y, SPI Lasers, UK) with a wavelength of 1064 nm and a pulse width of 7 ns. During laser irradiation, the RB-SiC surface was vertically irradiated by the laser beam with Gaussian energy distribution ($M^2 < 1.6$). The experiments were carried out under atmospheric conditions. The specific laser parameters are summarized in Table 1. Two sets of comparative experiments were designed to investigate the evolution of surface micro/nano structures formed by nanosecond pulsed laser irradiation, one in which the laser power was varied while other parameters remained constant, and the other in which the laser scanning speed was varied while keeping other parameters constant. After laser irradiation, the generated micro/nano structures were observed using a tungsten filament scanning electron microscope (SEM, JSM-IT500A, JEOL, Japan), and laser scanning confocal microscope (LSCM, OLS5100, Olympus, Japan) was used to photograph their three-dimensional (3D) topography. Energy dispersive X-ray spectrometer (EDS, EX-74600U4L2Q, JEOL, Japan), Raman microspectrometer (DXR3, Thermo Fisher Scientific, USA) and X-ray diffractometer (XRD, D8 Advance, Bruker, Germany) were performed to study the composition of the surface micro/nano structures. The contact angle of water with the surface was measured using an optical surface analyzer (OSA60, LAUDA Scientific, Germany), and the surface reflectivity was characterized by a spectrophotometer (PE lambda 750, America).

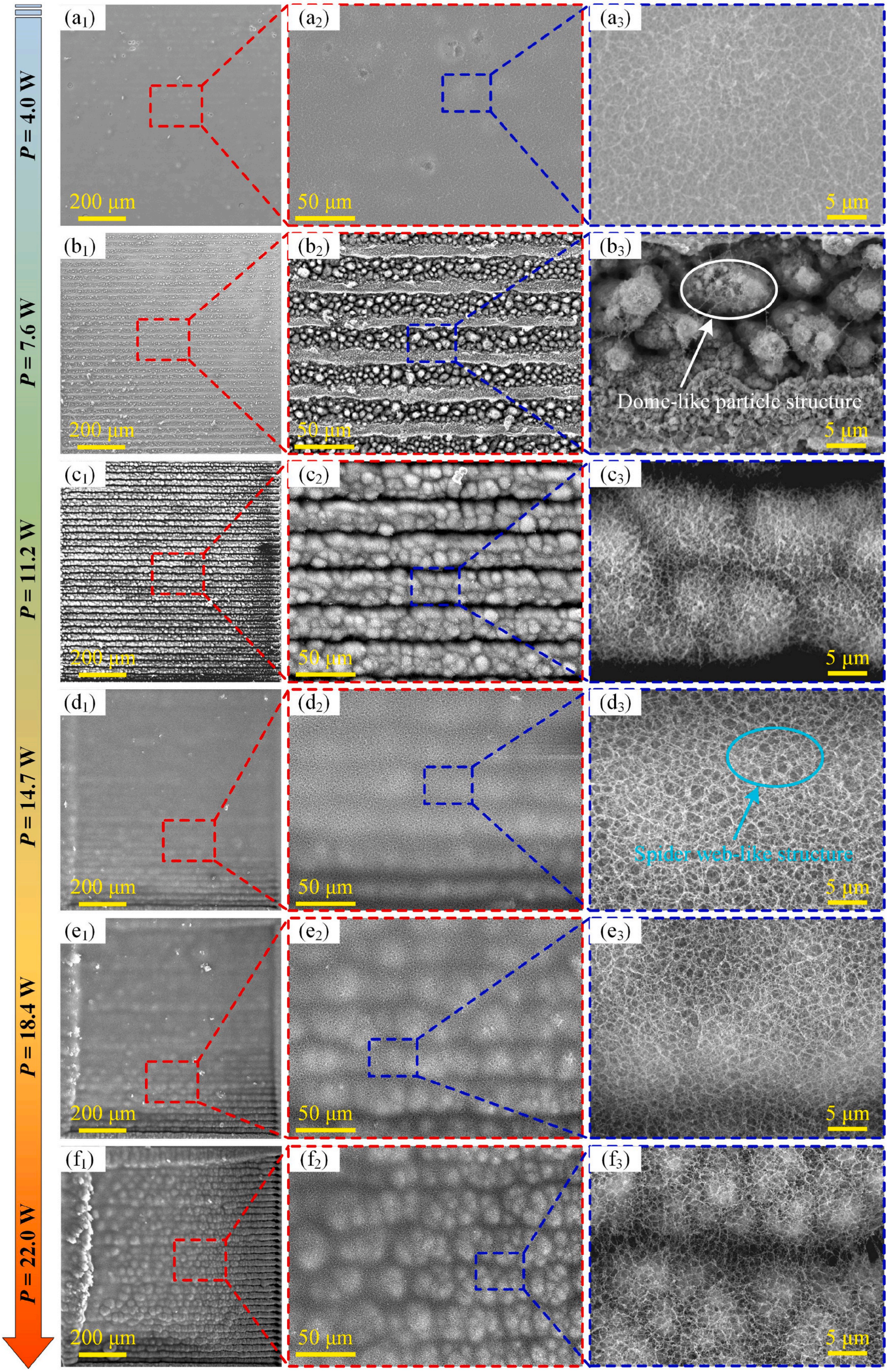

Fig. 2. SEM images of the micro/nano structures formed at various power levels: (a_1-a_3) 4.0 W; (b_1-b_3) 7.6 W; (c_1-c_3) 11.2 W; (d_1-d_3) 14.7 W; (e_1-e_3) 18.4 W; (f_1-f_3) 22.0 W.

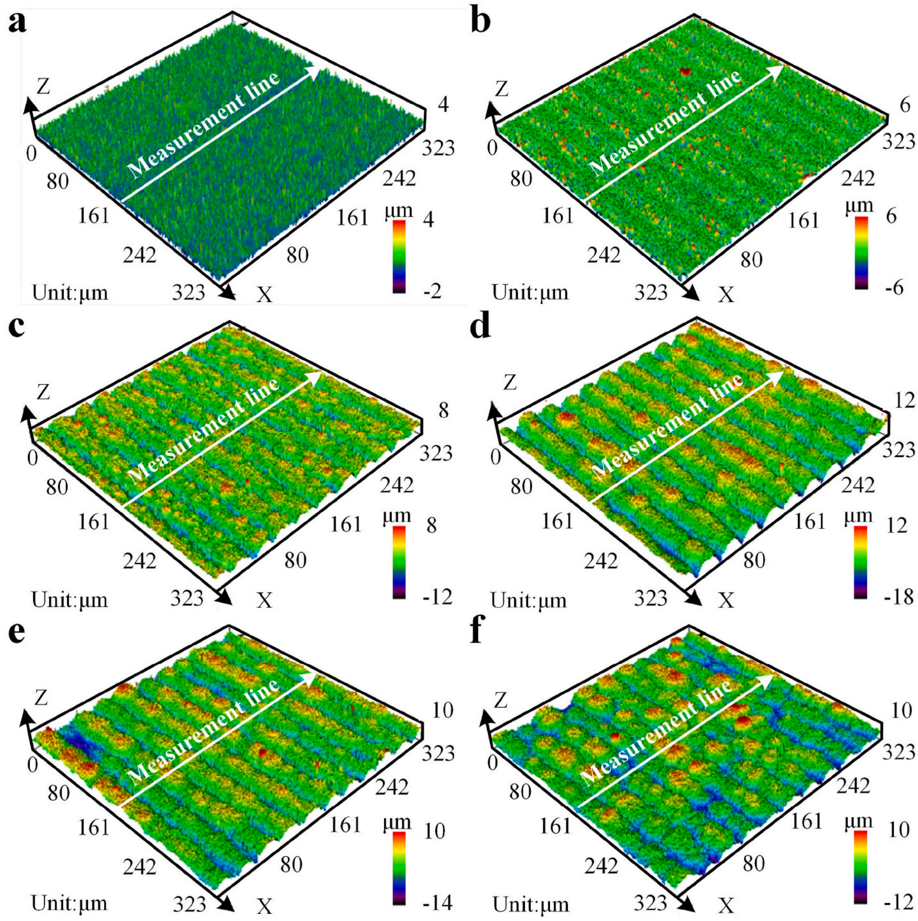

Fig. 3. 3D topographies of the micro/nano structures formed at various power levels: (a) 4.0 W; (b) 7.6 W; (c) 11.2 W; (d) 14.7 W; (e) 18.4 W; (f) 22.0 W.

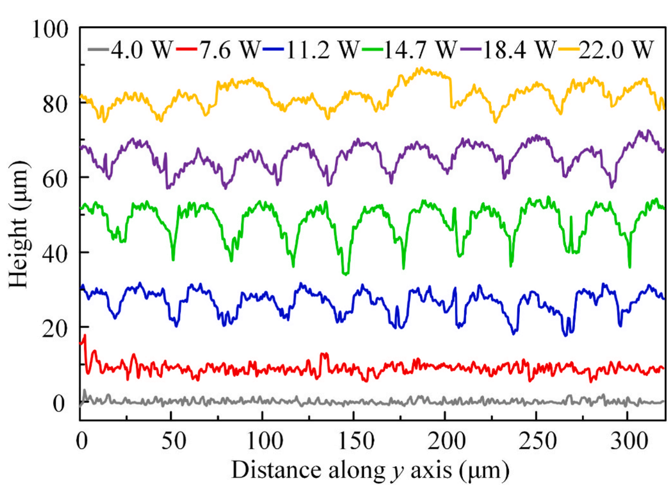

Fig. 4. The cross-sectional profile curves of the marked line in Fig. 3(a)-(f).

3. Results and discussion

3.1. Effects of laser parameters on the microscopic morphologies of micro/nano structures

Fig. 2 displays the scanning electron microscopy (SEM) images of the micro/nano structures formed at various laser power levels. When the surface is exposed to nanosecond laser irradiation at a relatively low laser power of 4.0 W, no visible laser irradiated tracks are detected, as observed in Fig. 2(a1) and (a2). However, when the laser power is increased to 7.6 W, an abundance of dome-like particle structures of varying sizes emerges on the RB-SiC surface (see Fig. 2(b2)). At the same time, narrow sheet structures are distributed on both sides. Further increasing the laser power results in the formation of periodic micro-cone structures on the surface, as demonstrated in Fig. 2(c1) and (c2). Interestingly, these micro-cone structures appear to be coated with a spider web-like film. It is worth noting that the thin spider web-like film

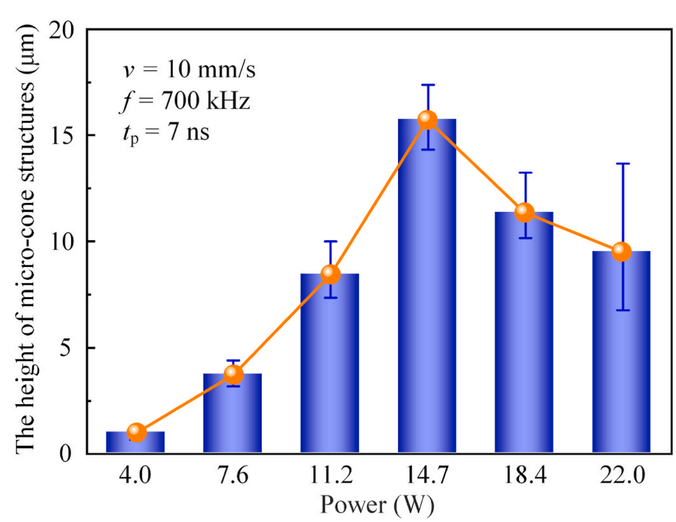

Fig. 5. Variations in the height of micro-cone structures as a function of the power.

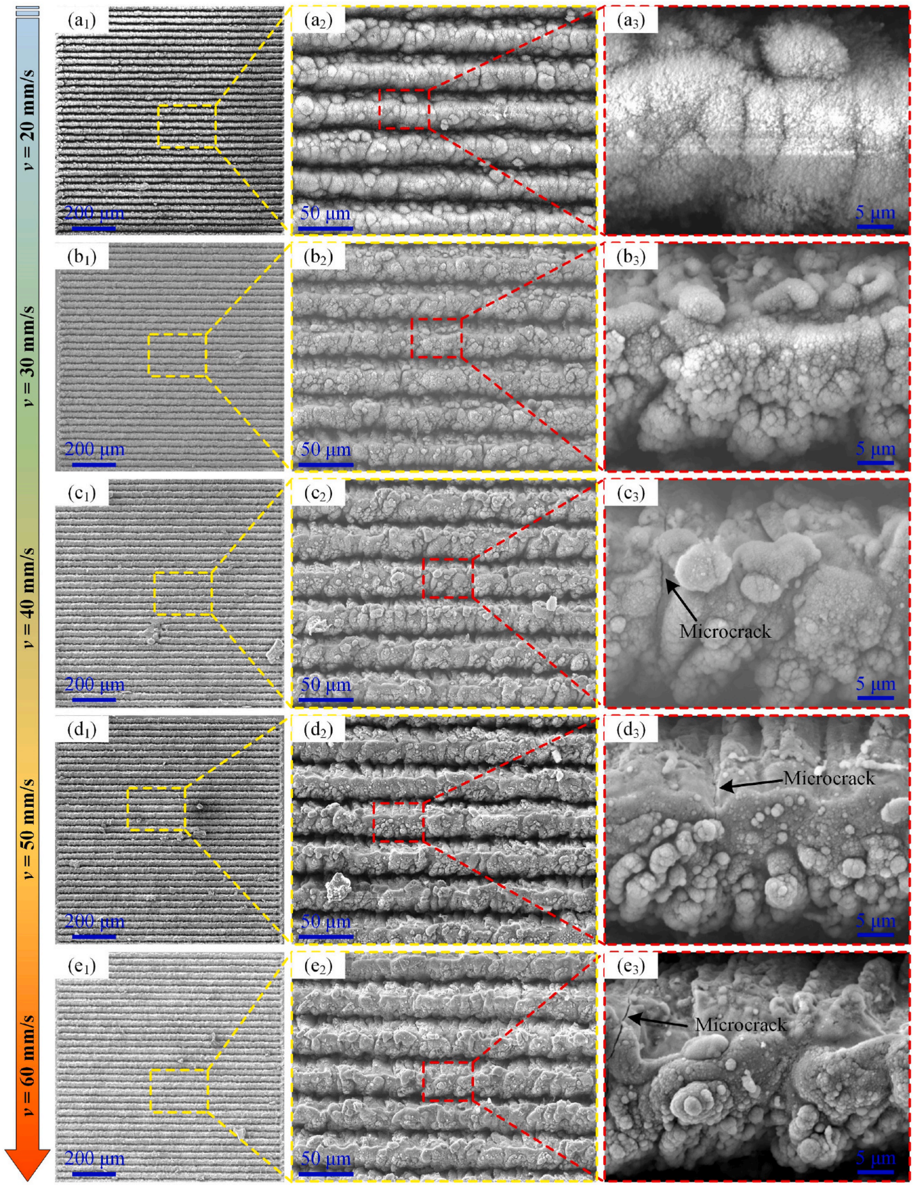

Fig. 6. SEM images of the micro/nano structures formed at different scanning speeds: (a_1-a_3) 20 mm/s; (b_1-b_3) 30 mm/s; (c_1-c_3) 40 mm/s; (d_1-d_3) 50 mm/s; (e_1-e_3) 60 mm/s.

only exists on the surface of the micro-cone structures and is not present in the pits on either side. When the laser power reaches to 14.7 W, compared to Fig. 2(c2), the underlying micro-cone structures become less discernible due to the presence of thicker spider web-like film that has formed on its top surface (Fig. 2(d2)). Furthermore, the pits on both sides of the micro-cone structures are also covered by the spider web-like film, as depicted in Fig. 2(d3). As the laser power is increased to 18.4 W or more, the spider web-like film on the top layer gradually weakens, and the micro-cone structures become more apparent, as illustrated in Fig. 2(e3) and (f3).

Fig. 3(a)-(f) presents the 3D topographies of the laser-irradiated regions corresponding to Fig. 2(a)-(f), respectively. Fig. 4 depicts the corresponding cross-sectional profile curves. It is evident that the nanosecond laser irradiation with a relatively low power (0~7.6 W) does not result in the formation of periodic micro-cone structures. Only when the power exceeds 11.2 W, relatively uniform micro-cone structures appear on the RB-SiC surface. The height of the micro-cone structures is measured to investigate the evolution of characteristic size in the surface micro/nano structures, and the results are shown in Fig. 5. The statistical data obtained from the cross-sectional profile indicate that as the laser power increases, the height of the micro-cone structures gradually increases to a maximum value of 15.73 μm, followed by a subsequent decrease, while the width gradually increases. A possible explanation for the initial increase in both the height and width of the micro-cone structures may be that the increased laser power causes more materials to melt and subsequently recast at the edge of the melt pool, with the corresponding formation of larger and wider micro-cone structures [29,30]. Furthermore, the subsequent decrease in the height of the micro-cone structures may be attributed to the evaporation of a large amount of molten material when the laser energy is excessively high [31–33].

Next, the influence of laser scanning speed on the formation and evolution of micro/nano structures is investigated and analyzed. Based on the previous discussion, it is found that nanosecond laser irradiation at a laser power of 14.7 W produces micro-cone structures with the greatest height, while higher laser energy will result in a large amount of materials being ablated and removed. To mitigate the ablation of RB-SiC surface under laser irradiation, the scanning speed for irradiating the

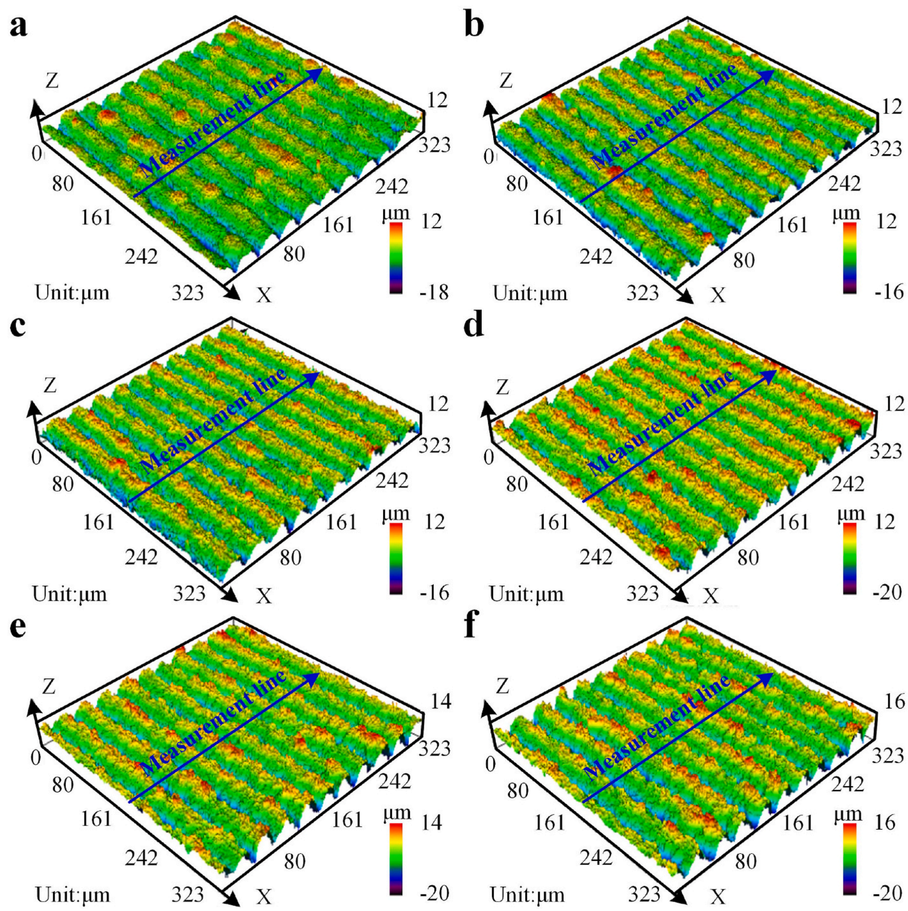

Fig. 7. 3D topographies of the micro/nano structures formed at different scanning speeds: (a) 10 mm/s; (b) 20 mm/s; (c) 30 mm/s; (d) 40 mm/s; (e) 50 mm/s; (f) 60 mm/s.

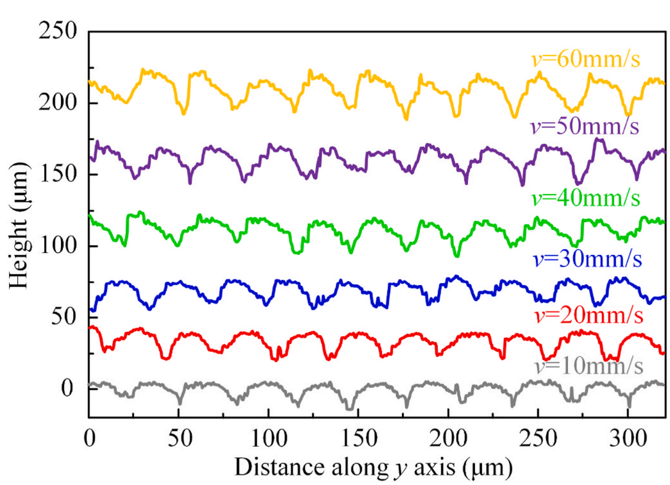

Fig. 8. The cross-sectional profile curves of the marked line in Fig. 7(a)-(f).

RB-SiC surface is increased in this study.

Fig. 6 depicts the SEM images of surface micro/nano structures obtained by laser irradiation at different scanning speeds. Combining Figs. 6 and 2, it is seen that when the scanning speed is equal to or higher than 20 mm/s, only micro-cone structures are formed on the RB-SiC surface and spider web-like film is not present. At the same time, particle structures with varying sizes are attached to the surface of micro-cone structures, exhibiting an irregular distribution.

Furthermore, when the scanning speed is set at 40-60 mm/s (Fig. 6 (c3)-(e3)), microcracks are observed on the laser irradiated regions. There are two main reasons for the emergence of these microcracks. On the one hand, after laser irradiation, an uneven distribution of heat leads to an uneven thermal expansion and high residual stress. When thermal stress exceeds the fracture strength of the RB-SiC, microcracks are formed to alleviate the stress [34]. On the other hand, RB-SiC is prone to surface and subsurface damage during the forming and machining processes, and the microcracks are prevalent [35,36]. These pre-existing microcracks cannot be fully filled and repaired by low-energy laser irradiation, and are exposed on the laser irradiated surface.

The 3D topographies and corresponding section profile curves of the micro/nano structures formed at different scanning speeds are depicted in Figs. 7 and 8, respectively. The experimental results indicate that nanosecond laser irradiation at all selected scanning speeds can induce the formation of periodic micro-cone structures. Additionally, the height of micro-cone structures decreases as the scanning speed decreases. This is due to the increased pulse overlap caused by the slower scanning speed, which results in more laser energy acting on the RB-SiC surface. Thus, a greater proportion of the molten material evaporates rather than being ejected outward to form micro-cone structures [29]. In addition, the decrease in scanning speed also prolongs the maintenance time of high irradiation temperature levels in the irradiated region, which may result in partial ablation and removal of the formed micro-cone structures [32]. The above results show that although the formation of periodic micro-cone structures does not depend on the laser scanning speed used, the change of scanning speed significantly affects the microscopic morphology and geometric dimension of the laser-induced micro/nano structures.

Table 2
Elemental composition of laser irradiated regions obtained under different power levels.

Element	C (at%)	O (at%)	Si (at%)
original	40.86	0	59.14
4.0 W	37.58	16.22	46.20
7.6 W	30.93	30.64	38.43
11.2 W	18.65	52.98	28.37
14.7 W	16.50	55.96	27.54
18.4 W	17.11	55.07	27.82
22.0 W	17.61	54.68	27.71

3.2. Characterization of chemical composition

As depicted in Fig. 2, distinct micro/nano structures were obtained by irradiating the RB-SiC surface in the air using a nanosecond laser at varying power levels. To investigate the chemical composition of these micro/nano structures, EDS regional analysis was conducted to determine the elemental composition of the regions shown in Fig. 2(a2)-(f2). The atomic content of each element is listed in Table 2, which provides valuable information regarding the composition of the micro/nano structures formed at various power levels. When the surface was irradiated by a nanosecond laser with relatively low power (0 - 7.6 W), the change in the carbon element was minimal, with only a slow decrease from 40.86% to 30.93%, as the laser power increases from 0 to 7.6 W. This suggests that low-energy laser irradiation does not induce significant decomposition of the SiC contained in RB-SiC, and only Si is ablated due to its low melting point. In contrast, when the laser power exceeds 11.2 W, the atomic element of C element is significantly reduced, and there is little disparity in the elemental composition of the laser irradiated regions. At the same time, it is essential to note that the atomic ratio of O/Si of surface micro/nano structures obtained by nanosecond laser irradiation with power ranging from 11.2 to 22.0 W is roughly 2:1, which suggests that SiO_2 may constitute the majority of the micro-cone structures and spider web-like film.

Furthermore, the elemental compositions of the laser irradiated regions shown in Fig. 6 (a2)-(e2) were acquired by EDS to investigate the effects of scanning speed on the chemical composition of the laser-induced micro/nano structures. It is seen from Fig. 9(a) that as the scanning speed increases, the content of C and Si elements decreases, while the content of O element shows an opposite trend, i.e., lower scanning speeds result in a higher degree of oxidation on the surface. To further investigate the chemical composition evolution induced by laser irradiation, the elements distribution along the marked line in Fig. 2(d2) was measured, and the corresponding results are shown in Fig. 9(b). The results demonstrate that the content of C element is negligible, whereas the variations in content of Si and O elements are closely correlated, which further support that the micro-cone structures mainly consist of silicon oxides. Fig. 9(c) displays the EDS mapping results of surface micro/nano structures formed at different scanning speeds. The Si and O elements are mainly enriched on the surface of the micro-cone structures, and their content is relatively low in the center of laser irradiated tracks. This may be due to the following reasons: during nanosecond laser irradiation, there might not be adequate time for oxygen molecules to effectively enter the irradiation center; On the other hand, due to the high energy density in the center of laser irradiated region, the generated silicon oxide may evaporate and be removed from the RB-SiC surface [32,37]. The above findings support the hypothesis that silicon oxides make up the majority of the micro-cone structures and offer important details about the distribution of elements and oxidation levels across the analyzed region.

The results of EDS tests show that laser irradiation of RB-SiC in air introduces oxygen on its surface, which may change its phase composition. To confirm this and further investigate the phase composition

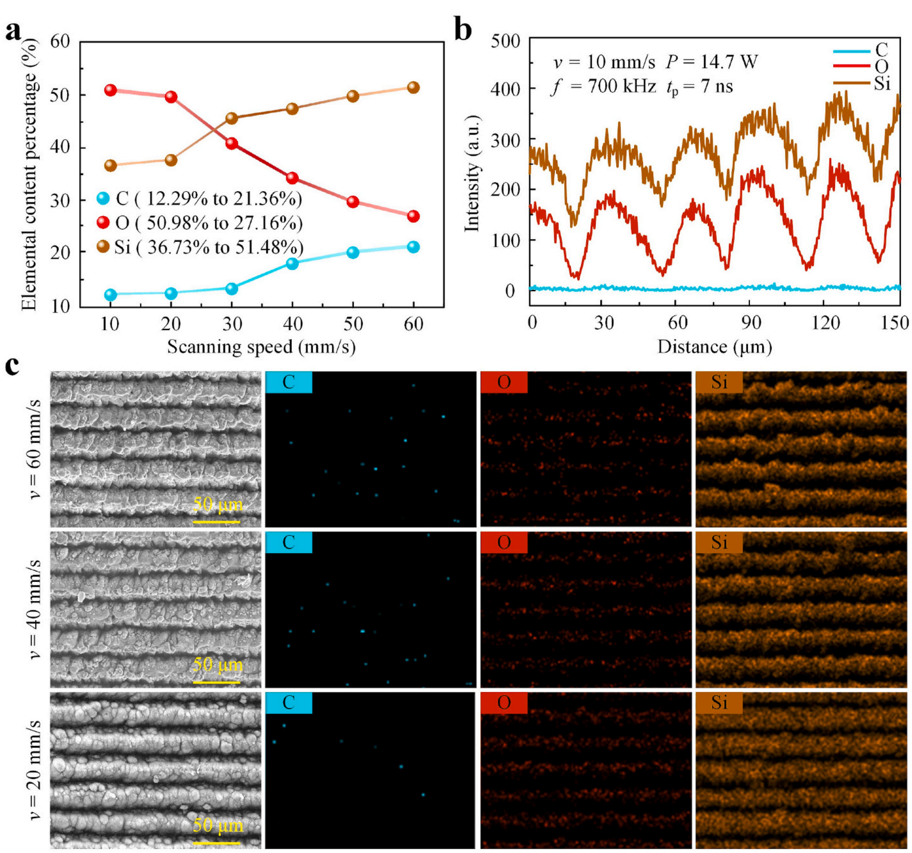

Fig. 9. (a) Variations in elemental content of the laser irradiated regions as a function of scanning speed. (b) Elements distribution along the marked line in Fig. 2 (d2). (c) EDS mapping results of surface micro/nano structures formed at different scanning speeds.

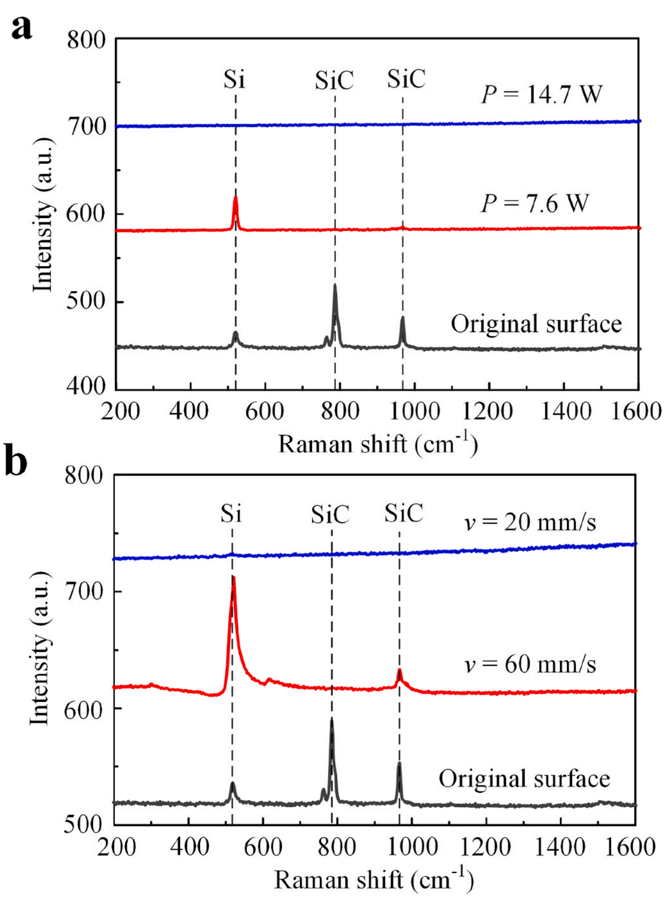

Fig. 10. Raman spectral curves of the micro/nano structures formed at different (a) powers and (b) scanning speeds.

evolution induced by laser irradiation, Raman tests were performed on various micro/nano structures, including the dome-like particle structures in Fig. 2(b2), the spider web-like film in Fig. 2(d3), and the micro-cone structures in Fig. 6(a3) and 6(e3). Fig. 10(a) presents the Raman spectral curves of these micro/nano structures. For comparison, the Raman spectral curve of the original surface is also included. As shown in Fig. 10(a), for the dome-like particle structures, a distinct peak is observed around 520 cm^{-1}, which corresponds to the monocrystalline silicon. This indicates that the dome-like particle structures primarily consist of Si. In addition, the peak intensity of the monocrystalline Si is higher than that of the original surface. To further illustrate the reasons for this phenomenon, a comparative analysis of the diameters of the Si matrix contained in the RB-SiC sample shown in Fig. 1(a) and the laser-induced dome-like particle structures illustrated in Fig. 2(b2) was performed. As shown in Fig. 11, the diameter of Si matrix contained in the RB-SiC sample is concentrated within the range of 1 μm, with an average size of approximately 0.588 μm. In contrast, the dome-like particle structures exhibit a concentration of diameters ranging from 2 to 6 μm, with an average size of roughly 5.601 μm. This difference in particle size indicates that Si generated from the decomposition of SiC and the original Si matrix contained in the RB-SiC sample works together to form dome-like particle structures, making its Raman peak intensity higher than that of the original surface. Being different from the Raman curve of the dome-like particle structures, the Raman curves of the spider web-like film do not exhibit any Raman peaks. Combined with the EDS test results presented in Fig. 9, it can be concluded that the spider web-like film is most likely composed of amorphous SiO_2.

Fig. 10(b) presents the Raman spectral curves of the micro/nano structures formed at different scanning speeds, which shows the same evolution law as the Raman spectral curves shown in Fig. 10(a). Compared to the original surface, the peak intensity of SiC phase in the laser-induced micro-cone structures obtained at a relatively high scanning speed (60 mm/s) decreases, while the peak associated with monocrystalline Si increases. This finding suggests that SiC is decomposed into Si and then recast to form micro-cone structures on the surface. As the scanning speed is further decreased, both the Si and SiC peaks disappear. This may be due to the molten Si reacting with oxygen in the air to form amorphous SiO_2, which then recasts to form micro/nano structures on the surface, resulting in the absence of detectable crystalline substances.

To confirm the presence of the amorphous SiO_2 and further demonstrate the effects of laser power and scanning speed on the phase composition of surface micro/nano structures, XRD tests were performed on the laser irradiated regions shown in Fig. 2(b2), 2(d2), 2(f2), and 6(c2). As illustrated in Fig. 12, the original RB-SiC surface primarily consists of 6H-SiC and Si. After irradiation with a nanosecond laser at different power levels or scanning speeds, the surface still contains 6H-SiC and Si, but their relative content varies with the laser parameters. For instance, compared to the original surface, when the laser power of 7.6 W or scanning speed of 60 mm/s is applied, the content of 6H-SiC decreases while the content of Si increases. This observation provides further confirmation that SiC undergoes melting and decomposition at high temperatures. Further increasing the power to 14.7 W or decreasing the scanning speed to 10 mm/s results in a further reduction in the peak intensities of 6H-SiC and Si phases. Additionally, a low-intensity characteristic peak of amorphous SiO_2 is observed near $2\theta = 22^{\circ}$ in the XRD spectrum [38]. This phenomenon suggests that increasing the power or decreasing the scanning speed causes more melting and decomposition of 6H-SiC, resulting in the generation of more molten Si. The molten Si then reacts with oxygen in the air, resulting in the formation of SiO_2. When the power is further increased to 22.0 W, the intensity of 6H-SiC, Si, and amorphous SiO_2 exhibits a slightly decreasing trend. This could be attributed to the increased laser energy acting on the surface, which

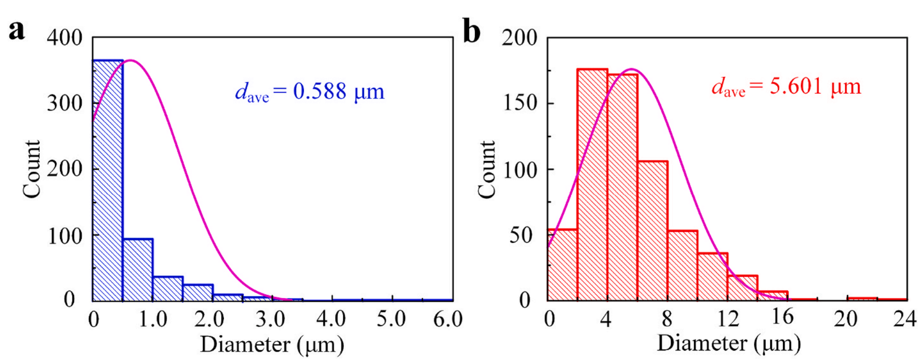

Fig. 11. Histogram of particle diameter: (a) silicon matrix shown in Fig. 1(a); (b) dome-like particles illustrated in Fig. 2(b_2). (For interpretation of the references to colour in this figure legend, the reader is referred to the Web version of this article.)

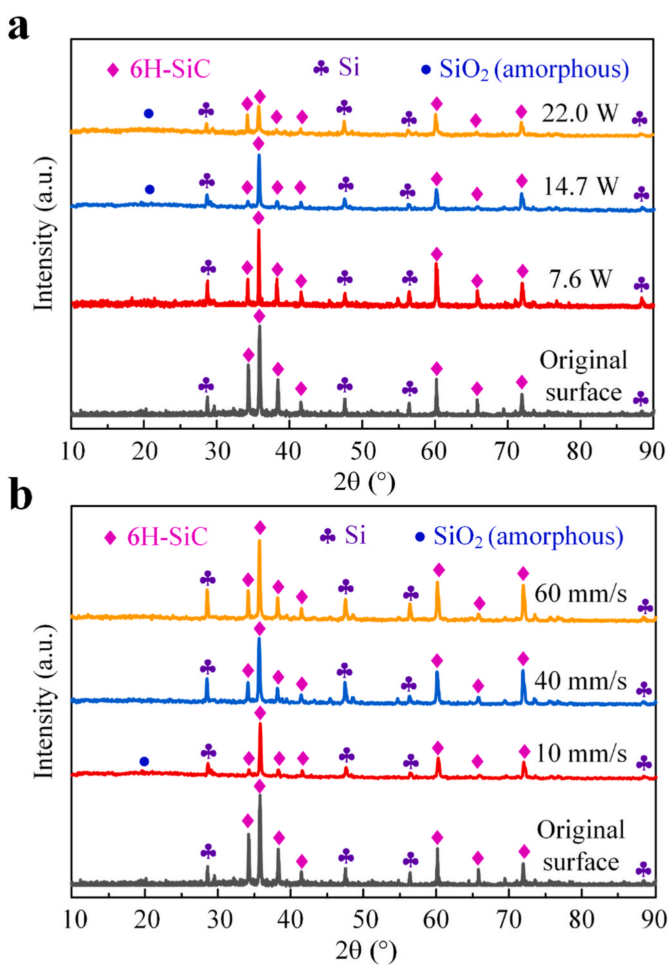

Fig. 12. XRD patterns of the micro/nano structures formed at (a) different powers and (b) scanning speeds.

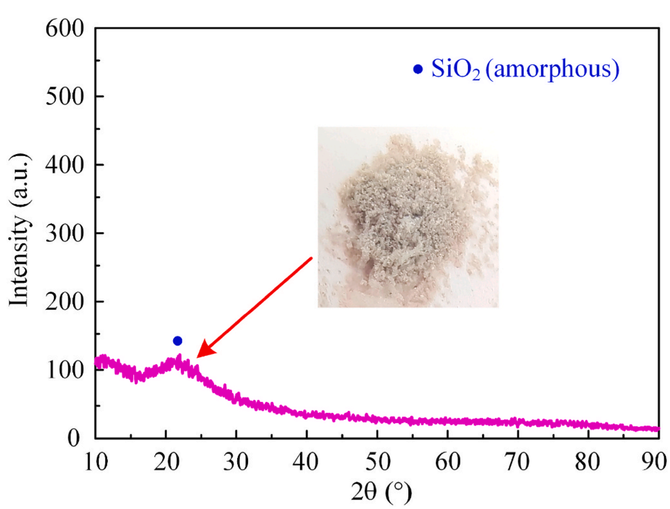

Fig. 13. XRD pattern of the powder scraped off the laser irradiated region.

causes the melting and decomposition of a small number of large-scale 6H-SiC. Additionally, a significant amount of Si and SiO_2 formed through bonding and reaction evaporates at high temperatures. Since the white amorphous SiO_2 layer covered on the micro-cone structures may be very thin and thus difficult to detect by XRD, it was scraped from the laser irradiated regions and then collected as white powders for XRD testing. The corresponding results are shown in Fig. 13, where a broad and diffuse scattering peak is identified as SiO_2.

Based on the above test results, the correlation between the content of the ablation products and the laser parameters could be established. Under relatively weak laser energy, the ablation products formed on the RB-SiC surface primarily consist of Si, which exists in the form of micro-cone structures and dome-like particle structures. As the laser power or scanning speed is adjusted to increase the laser energy, the predominant ablation products become amorphous SiO_2, which can be observed in the form of micro-cone structures, particle structures, and spider web-like film. Even when the laser energy is further increased, the ablation products still mainly consist of SiO_2. However, at this stage, their concentration reduces significantly, perhaps as a result of the evaporation and dissipation of partially melted materials at high temperatures.

3.3. Mechanism of laser ablation of RB-SiC

During laser ablation of RB-SiC, a variety of intricate interactions occur between them, involving physical process such as material decomposition, evaporation, ejection and solidification of the molten substances. Fig. 14 depicts the interaction process and mechanism between laser and RB-SiC material. As shown in Fig. 14(a), the nanosecond pulsed laser generates spot energy with a Gaussian distribution. When the laser irradiates the RB-SiC surface, the laser energy is absorbed due to the photothermal effect [39], resulting in rapid heating and melting of the RB-SiC. Initially, when the local temperature is insufficient to melt the material, no visible laser irradiated track appears on the RB-SiC surface, as depicted in Fig. 2(a2). As the temperature continues to increase, the SiC starts to decompose into solute carbon and liquid silicon [40]. As the temperature further increases, more material melts, leading to the expansion of the molten pool. At the same time, the heat is transferred to the surrounding region. When the temperature of the molten pool exceeds the evaporation temperature of the RB-SiC, large amounts of Si and SiC vaporize and create a gaseous vapor cloud above the molten pool, as illustrated in Fig. 14(b). This vapor cloud generates recoil pressure on the molten pool [41], which propels the movement of molten materials from the center towards the periphery of the pool. Additionally, Marangoni convection is also an important factor influencing the flow of molten materials, which is related to the surface tension. It causes the molten materials to flow from regions of low surface tension to regions of high surface tension. Previous studies [29, 42] have demonstrated an inverse relationship between surface tension and temperature. Due to the Gaussian energy distribution of the laser beam, the temperature distribution in the melt pool is uneven, with the highest temperature in the central region and the lowest temperature in the edge region. As a result, Marangoni convection pushes the molten materials from the center of the melt pool towards its edges. Moreover, the flow of molten material is also influenced by gravity. The effect of gravity, in contrast to Marangoni convection, is to hinder the outward flow of molten materials. When the laser energy is relatively low, the combined effect of recoil pressure and Marangoni convection is insufficient to overcome the gravity. As a result, the molten materials are expelled and recast in the pits, forming dome-like particle structure depicted in Fig. 2(b3). As the laser energy increases, the enhanced recoil pressure and Marangoni convection enable a backward outward flow against the gravity, causing the molten materials to cold cast on the surface and form micro-cone structures, as seen in Fig. 2(c3). At this stage, the intensified recoil pressure directly expels a portion of the molten material from the molten pool onto the surface, leading to the formation of particle structures with varying sizes, as illustrated in Fig. 6 (c3). In Fig. 14(c), when the laser energy is relatively high, the molten materials in the pool flow towards the edge and recasts, resulting in the formation of micro-cone structures. Simultaneously, two chemical reactions occur. First, a large amount of molten carbon vaporizes and combines with oxygen in the air, producing carbon monoxide or carbon dioxide that dissipates into the atmosphere. Second, a significant

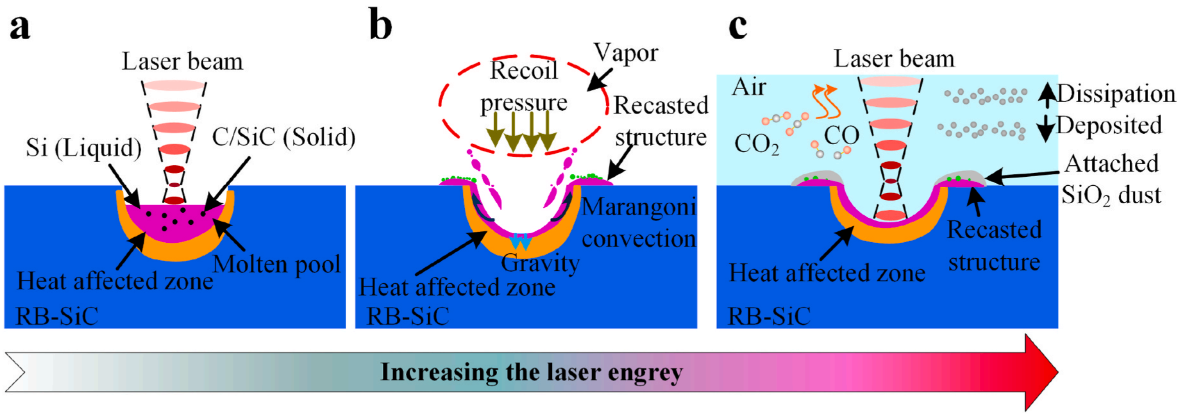

Fig. 14. Schematic diagram illustrating the mechanism of laser ablation of RB-SiC.

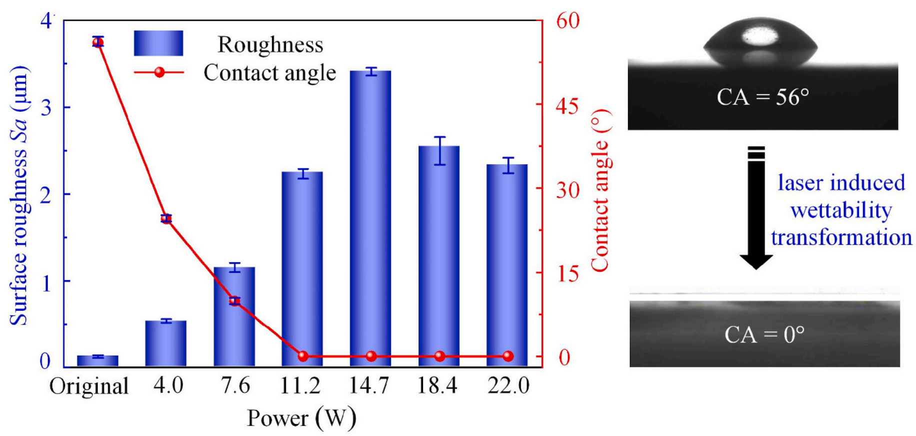

Fig. 15. The contact angle test results as well as the surface roughness of the original and laser irradiated surfaces.

amount of silicon in the molten pool evaporates at high temperatures to from Si vapor, which chemically interacts with oxygen to produce amorphous SiO_2. These SiO_2 particles primarily exist as very fine particles. Some SiO_2 particles dissipate into free space due to their initial kinetic energy [43]. The remaining particles fall back onto the recast surface under atmospheric pressure and gravity, subsequently forming a thin layer composed of SiO_2 (i.e., spider web-like film), as shown in Fig. 2(d3)- (f3).

3.4. Surface wettability

It has been established that the surface micro/nano structures have a considerable impact on the surface wettability [44–46]. A 1 μL droplet of deionized water was employed to investigate the influence of the micro/nano structures on the surface wettability behavior of the RB-SiC surface. Fig. 15 shows the contact angle test results as well as the surface roughness of the original and laser irradiated surfaces. The contact angle of the original surface is approximately 56°. As the laser power increases, the contact angle decreases. Once the laser power exceeds 11.2 W, the surface exhibits superhydrophilicity, with a contact angle of 0°. From Fig. 15, it can be observed that as the laser power increases within the range of 0-14.7 W, the surface roughness gradually increases. However, once the applied power exceeds 14.7 W, the surface roughness shows a decreasing trend. The calculation of the apparent contact angle based on Wenzel's mode can be performed using the following approach [47]:

$$\cos\theta = r\cos\theta_0 \tag{3-1}$$

Where the roughness factor r is defined as the ratio of the absolute

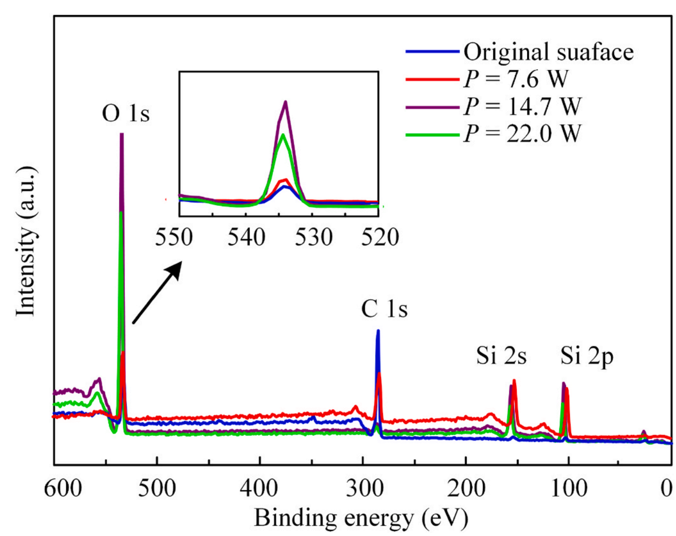

Fig. 16. XPS spectra patterns of the original and laser irradiated surfaces.

surface area to the projected area, the contact angle θ represents the angle formed between the water droplet and the textured surface, and θ_0 denotes the contact angle on a smooth surface. The increase in surface roughness increases the contact regions between water and the surface. This increased contact area facilitates the diffusion of water droplets on the surface [48]. Another important reason is that the micro-cone structures and the spider web-like film make it easier for water

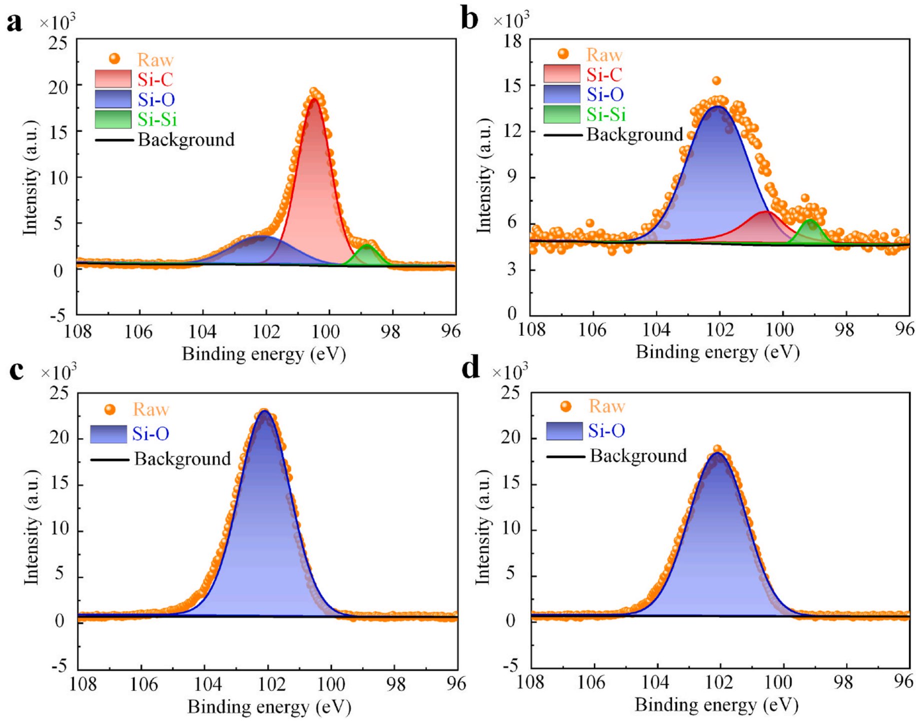

Fig. 17. The high-resolution core-level spectra of Si2p of laser irradiated surfaces with various power levels: (a) original surface; (b) 7.6 W; (c) 14.7 W; (d) 22.0 W.

droplets to flow and dissipate on the RB-SiC surface due to their large specific surface area.

To further investigate the reasons for the superhydrophilicity of the modified RB-SiC surface, X-ray photoelectron spectroscopy (XPS) tests were conducted on the laser-irradiated regions depicted in Fig. 2(b2), (d2), and (f2). The corresponding XPS spectra patterns are shown in Fig. 16, and the presence of Si, C, and O lines in the analyzed regions can be observed. As the laser power increases, the O content initially rises and then falls, but remains higher than that of the original surface. Numerous studies [49,50] have consistently shown that an increase in O content contributes to improving the hydrophilicity of the material surface. Fig. 17 exhibits the high-resolution core-level spectra of Si2p. The Si element primarily exists in the forms of Si-O (102.1 eV), Si-C (100.4 eV), and Si-Si (98.9 eV) on the original RB-SiC surface [51]. Upon irradiation of the RB-SiC surface with a nanosecond laser at 7.6 W, the intensity of the Si-O bond increases significantly, leading to a remarkable reduction in the contact angle from 56° to 9.8°. When the power exceeds 14.7 W, the intensity of the Si-O bond exhibits a sharp rise, and only the Si-O bond is present in the Si2p spectrum. As a result, the contact angle maintains a constant value of 0°. Moreover, the presence of SiO_2, with its high surface energy, plays a crucial role in maintaining stable wetting behavior [52]. These testing results indicate that nanosecond laser irradiation can induce the transition from hydrophilicity to superhydrophilicity, which can be attributed to a combination action of surface micro/nano structures and chemical composition. The preparation of superhydrophilic surfaces is expected to expand the application prospects of RB-SiC materials, such as anti-fogging, anti-fouling, and directional fluid transportation.

3.5. Optical characteristics

The reflectivity of material has a significant influence in determining its ablative properties. To explore the effects of fabricated micro/nano structures on the reflectivity of the RB-SiC surface, reflectivity tests were carried on the surfaces depicted in Fig. 2(b1) and 2(d1). In addition, the reflectivity of the laser irradiated surface shown in Fig. 2(d1) scraped off the spider web-like film was also tested to demonstrate the effect of SiO_2 on the reflectivity. The reflectivity test results on the above-mentioned surfaces are shown in Fig. 18. The results demonstrate varying degrees of increased reflectivity on the irradiated surface. Particularly, the reflectivity of the surface irradiated by a nanosecond laser with a power of 14.7 W exhibits an increase of 83% or more in the wavelength range of 200 to 2500 nm. This increase in reflectivity can be attributed to the presence of dome-like particle structures and the dense SiO_2 film, which act as barriers for incident light wave. Furthermore, the high reflectivity of SiO_2 itself plays a significant role in enhancing the overall reflective properties. In addition, removal of the spider web-like film from the laser irradiated surface results in a significant decrease in reflectivity, even slightly below that of the original surface. In addition to the removal of high-reflectivity SiO_2 films, the reflectivity of the laser irradiated surface after scraping is lower than that of the original surface may be due to the difference in surface roughness. Fig. 19 displays the 3D morphologies of the original surface and the laser irradiated surface

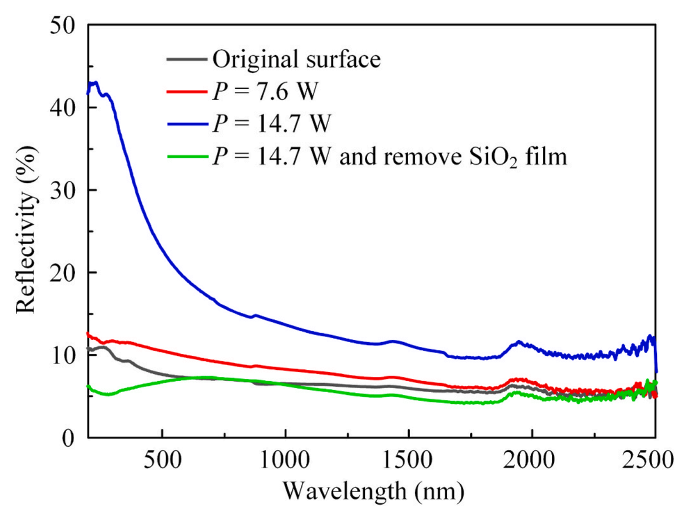

Fig. 18. Reflectivity of the original and laser irradiated surfaces.

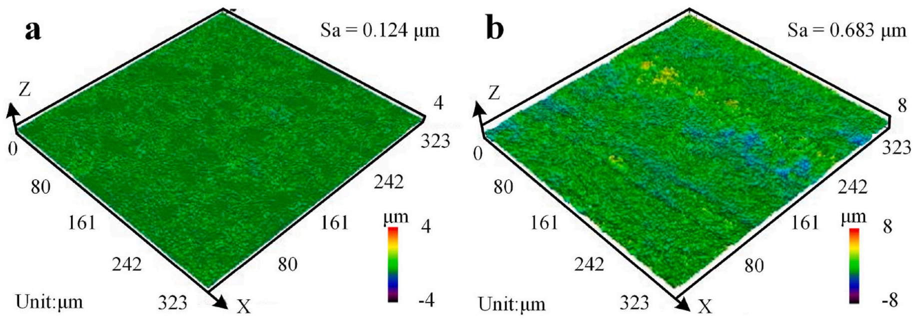

Fig. 19. Three-dimensional morphologies. (a) original surface; (b) laser irradiated surface after scraping.

after scraping, where the laser-irradiated surface after scraping exhibits a higher surface roughness. The increased surface roughness leads to stronger diffuse reflection of light, resulting in a slightly lower reflectivity compared to the original surface.

4. Conclusions

In summary, the RB-SiC surface was irradiated by a nanosecond pulsed laser with various experimental conditions in an atmospheric environment, and the surface micro/nano structures, chemical composition, surface wettability, and surface reflectivity of the laser irradiated surfaces were characterized and comparatively analyzed in detail. The main conclusions are as follows:

(1) As laser power increased and the energy reached the ablation threshold of RB-SiC, various micro/nano structures gradually developed on the RB-SiC surface, including dome-like particle structures, micro-cone structures, and the spider web-like film.
(2) The change of laser scanning speed does not affect the formation of uniform micro-cone structures, however, there were significant differences in surface morphology and element composition. In both EDS and XRD measurements, a variety of levels of ablation and oxidation are observed on the surface under laser irradiation at varying scanning speeds. Low scanning speeds result in more ablation of material and high oxygen content.
(3) The formation of micro-cone structures is the result of the rapid solidification of the molten material after it is pushed upward to the surface under the action of recoil pressure and Marangoni flow. Spider web-like films are generated as a result of oxidation of silicon vapor initially which was then deposited on the micro-cone structures due to atmospheric pressure and gravity.
(4) The micro-cone structures are mainly composed of Si and SiO_2. The O element content of micro-cone structures irradiated by nanosecond pulsed laser with different parameters is different. Moreover, the spider web-like film is composed of SiO_2 and dome-like particle structures are mainly composed of Si.
(5) Compared to the original surface, the hydrophilicity of the laser irradiated surface is enhanced, even reaches superhydrophilicity, which can be attributed to the increased specific surface area associated with the formation of the micro/nano structures as well as the existence of SiO_2 components.
(6) The dense SiO_2 film is conducive to blocking of laser incidence, resulting in a surface reflectivity increase of 83% or more compared to the original surface. In addition, after removing the SiO_2 film, the surface reflectivity can be restored to the same level of the original surface.

Data availability statement

The data that support the findings of this study are available from the corresponding author upon reasonable request.

Declaration of competing interest

The authors declare that they have no known competing financial interests or personal relationships that could have appeared to influence the work reported in this paper.

Acknowledgements

This work was supported by the Natural Science Foundation of Jilin Province (20220101198JC), the National Key Research and Development Plan Project (Grant No. 2022YFB4600204), and the Fundamental Research Funds for the Central Universities (2020-2023).

References

[1] P.S. Grinchuk, M.V. Kiyashko, H.M. Abuhimd, M.S. Alshahrani, D.V. Solovei, M. O. Stepkin, A.V. Akulich, M.D. Shashkov, T.A. Kuznetsova, S.M. Danilova-Tretiak, L.E. Evseeva, K.V. Nikolaeva, Advanced technology for fabrication of reaction-bonded SiC with controlled composition and properties, J. Eur. Ceram. Soc. 41 (2021) 5813–5824.
[2] X. Rao, F. Zhang, X. Luo, F. Ding, Y. Cai, J. Sun, H. Liu, Material removal mode and friction behaviour of RB-SiC ceramics during scratching at elevated temperatures, J. Eur. Ceram. Soc. 39 (2019) 3534–3545.
[3] H.-W. Sung, Y.-H. Kim, D.J. Kim, Joining of reaction bonded silicon carbide using self-infiltration of residual Si present in the RBSC, Ceram. Int. 46 (2020) 28800–28805.
[4] Z. Zhang, P. Yao, J. Wang, C. Huang, H. Zhu, H. Liu, B. Zou, Nanomechanical characterization of RB-SiC ceramics based on nanoindentation and modelling of the ground surface roughness, Ceram. Int. 46 (2020) 6243–6253.
[5] Y. Zou, C.-H. Li, Y. Tang, L. Hu, J.-A. Liu, J.-M. Wu, Y.-S. Shi, Preform impregnation to optimize the properties and microstructure of RB-SiC prepared with laser sintering and reactive melt infiltration, J. Eur. Ceram. Soc. 40 (2020) 5186–5195.
[6] F. Sadegh Moghanlou, S. Nekahi, M. Vajdi, Z. Ahmadi, A. Motallebzadeh, A. Shokouhimehr, M. Shokouhimehr, S. Jafargholinejad, M. Shahedi Asl, Effects of graphite nano-flakes on thermal and microstructural properties of TiB_2–SiC composites, Ceram. Int. 46 (2020) 11622–11630.
[7] X. Zhang, W. Xie, L. Sun, Z. Wei, Z. Zhang, Y. Zhu, J. Hu, S. Wang, Z. Shi, Continuous SiC skeleton reinforced highly oriented graphite flake composites with high strength and specific thermal conductivity, Journal of Advanced Ceramics 11 (2022) 403–413.
[8] X. Zhou, L. Jing, Y.D. Kwon, J.-Y. Kim, Z. Huang, D.-H. Yoon, J. Lee, Q. Huang, Fabrication of SiCw/Ti3SiC2 composites with improved thermal conductivity and mechanical properties using spark plasma sintering, Journal of Advanced Ceramics 9 (2020) 462–470.
[9] S. Caruso, G. Ambrogio, Novel drawing system approach to manufacture performant commercially pure aluminium fine wires, Int. J. Adv. Des. Manuf. Technol. 118 (2021) 1101–1109.
[10] P. Kurnsteiner, M.B. Wilms, A. Weisheit, B. Gault, E.A. Jagle, D. Raabe, High-strength Damascus steel by additive manufacturing, Nature 582 (2020) 515–519.
[11] T.M. Smith, C.A. Kantzos, N.A. Zarkevich, B.J. Harder, M. Heczko, P.R. Gradl, A. C. Thompson, M.J. Mills, T.P. Gabb, J.W. Lawson, A 3D printable alloy designed for extreme environments, Nature 617 (2023) 513–518.
[12] W. Xu, L. Gao, C. Ma, Z. Ma, T. Wu, A.A. Rogachev, F. Wang, Design and preparation of composite coatings with increased reflectivity under high-energy continuous wave laser ablation, Ceram. Int. 46 (2020) 23457–23462.
[13] L.B. Kong, C.F. Cheung, S. To, C.T. Cheng, Modeling and characterization of generation of 3D micro-structured surfaces with self-cleaning and optical functions, Optik - International Journal for Light and Electron Optics 124 (2013) 2848–2853.
[14] Y. Wenxuan, Y. Yuan, L. Guoyong, Z. Bing, Y. Rongkai, The anti-icing/frosting aluminum surface with hydrangea-like micro/nano structure prepared by chemical etching, Mater. Lett. 226 (2018) 4–7.

[15] X. Rao, F. Zhang, Y. Lu, X. Luo, F. Ding, C. Li, Analysis of diamond wheel wear and surface integrity in laser-assisted grinding of RB-SiC ceramics, Ceram. Int. 45 (2019) 24355–24364.
[16] B. Xu, P. Jiang, Y. Wang, J. Zhao, S. Geng, Heat-mass transfer and its effects on the in-situ Al/SiC reactions in aluminum welds during wobbling laser melting injection of SiC particles, J. Mater. Process. Technol. 308 (2022) 117707–117723.
[17] T. Meshram, J. Yan, Generation of microcones on reaction-bonded silicon carbide by nanosecond pulsed laser irradiation, Int. J. Adv. Des. Manuf. Technol. 108 (2019) 1039–1048.
[18] J.-P. Chen, L. Gu, G.-J. He, A review on conventional and nonconventional machining of SiC particle-reinforced aluminium matrix composites, Advances in Manufacturing 8 (2020) 279–315.
[19] Y. Qian, H. Huang, M. Jiang, J. Yan, Nanosecond pulsed laser-induced formation of nanopattern on Fe-based metallic glass surface, Appl. Surf. Sci. 577 (2022) 151976–151984.
[20] N. Thawari, C. Gullipalli, A. Chandak, T.V.K. Gupta, Influence of laser cladding parameters on distortion, thermal history and melt pool behaviour in multi-layer deposition of stellite 6: in-situ measurement, J. Alloys Compd. 860 (2021) 157894–157905.
[21] S. Debnath, S. Kunar, S.S. Anasane, B. Bhattacharyya, Non-traditional micromachining processes: opportunities and challenges, Non-traditional Micromachining Processes (2017) 1–59.
[22] N. Haustrup, G.M. O'Connor, The influence of thin film grain size on the size of nanoparticles generated during UV femtosecond laser ablation of thin gold films, Appl. Surf. Sci. 278 (2013) 86–91.
[23] J. Yong, Q. Yang, F. Chen, X. Hou, Femtosecond laser-induced superwetting surfaces, Chin. Sci. Bull. 64 (2018) 1213–1237.
[24] D. Lou, B. Wang, E. Liang, G. Lu, J. Cheng, J. Liao, Q. Yang, D. Liu, Effect of heat treatment on wettability and condensation heat transfer of laser-textured stainless steel surfaces, Phys. Status Solidi 219 (2021) 2100458–2100465.
[25] A.F. Mohammed, Q.A. Al-Jarwany, A.J. Clarke, T.M. Amaral, J. Lawrence, N. T. Kemp, C.D. Walton, Ablation threshold measurements and surface modifications of 193 nm laser irradiated 4H-SiC, Chem. Phys. Lett. 713 (2018) 194–202.
[26] S.I. Sadovnikov, E.G. Vovkotrub, Thermal stability of nanoparticle size and phase composition of nanostructured Ag2S silver sulfide, J. Alloys Compd. 766 (2018) 140–148.
[27] F. Yang, Z. Dong, R. Kang, C. Liu, D. Wu, G. Ma, Laser ablation of RB-SiC composite by femtosecond laser irradiation, Optik 273 (2023) 170509–170523.
[28] T. Meshram, J. Yan, Formation of laser-induced periodic surface structures on reaction-bonded silicon carbide by femtosecond pulsed laser irradiation, Nanomanufacturing and Metrology 6 (2023) 4–16.
[29] S. Feng, R. Zhang, C. Huang, J. Wang, Z. Jia, J. Wang, An investigation of recast behavior in laser ablation of 4H-silicon carbide wafer, Mater. Sci. Semicond. Process. 105 (2020) 104701–104712.
[30] R. Zhang, C. Huang, J. Wang, D. Chu, D. Liu, S. Feng, Experimental investigation and optimization of femtosecond laser processing parameters of silicon carbide–based on response surface methodology, Ceram. Int. 48 (2022) 14507–14517.
[31] Y. Deng, Y. Zhou, Y. Zhang, D. Chen, X. Zhou, Numerical and experimental analysis of nanosecond laser ablation of SiC, Mater. Sci. Semicond. Process. 151 (2022) 107020–107025.
[32] C. Fu, Y. Yang, Z. Huang, G. Liu, H. Zhang, F. Jiang, Y. Wei, Z. Jiao, Investigation on the laser ablation of SiC ceramics using micro-Raman mapping technique, Journal of Advanced Ceramics 5 (2016) 253–261.
[33] C. Liu, C. Li, L. Gao, R. Shen, Micro-hole drilling of 2.5D C/SiC composite with picosecond laser: numerical modeling and experimental validation on hole shape evolution, J. Manuf. Process. 81 (2022) 852–864.
[34] J. Lu, Y. Dang, J. Huang, Y. Zhou, Z. Yang, J. Yan, Y. Yuan, Y. Gu, Preparation and characterization of slurry aluminide coating on Super304H boiler tube in combination with heat-treatment process, Surf. Coating. Technol. 370 (2019) 97–105.
[35] N. Furushiro, M. Higuchi, T. Yamaguchi, S. Shimada, K. Obata, Polishing of single point diamond tool based on thermo-chemical reaction with copper, Precis. Eng. 33 (2009) 486–491.
[36] J. Yan, T. Asami, T. Kuriyagawa, Response of machining-damaged single-crystalline silicon wafers to nanosecond pulsed laser irradiation, Semicond. Sci. Technol. 22 (2007) 392–395.
[37] D.V. Feoktistov, G.V. Kuznetsov, A.A. Sivkov, A.S. Ivashutenko, D.S. Nikitin, I. I. Shanenkov, A.M. Abdelmagid, E.G. Orlova, Expanding the scope of SiC ceramics through its surface modification by different methods, Surf. Coating. Technol. 435 (2022) 188263–188277.
[38] J. Chen, Q. An, W. Ming, M. Chen, Investigations on continuous-wave laser and pulsed laser induced controllable ablation of SiC_f/SiC composites, J. Eur. Ceram. Soc. 41 (2021) 5835–5849.
[39] J.Y. Lu, H.A. Chen, C.M. Yang, L.K. Chu, Radiative relaxation of gold nanorods coated with mesoporous silica with different porosities upon nanosecond photoexcitation monitored by time-resolved infrared emission spectroscopy, ACS Appl. Mater. Interfaces 13 (2021) 60018–60026.
[40] B. Adelmann, R. Hellmann, A study of SiC decomposition under laser irradiation, Appl. Phys. A 123 (2017) 454–459.
[41] K. Li, H. Zhou, Z. Zhao, H. Zhou, J. Yin, J. Jin, A study on transient molten pool dynamics in laser polishing of Ti6Al4V using numerical simulation, J. Manuf. Process. 65 (2021) 478–490.
[42] Y. Qian, M. Jiang, Z. Zhang, H. Huang, J. Yan, On the transformation between micro-concave and micro-convex in nanosecond laser ablation of a Zr-based metallic glass, J. Manuf. Process. 68 (2021) 1114–1122.
[43] J. Long, Z. He, P. Zhou, X. Xie, C. Zhou, W. Hong, W. Hu, Low-cost fabrication of large-area broccoli-like multiscale micro- and nanostructures for metallic super-hydrophobic surfaces with ultralow water adhesion and superior anti-frost ability, Adv. Mater. Interfac. 5 (2018) 1800353–1800360.
[44] M. Cui, H. Huang, C. Wang, L. Zhang, J. Yan, Achieving superhydrophobicity of Zr-based metallic glass surfaces with tunable adhesion by nanosecond laser ablation and annealing, ACS Appl. Mater. Interfaces 14 (2022) 39567–39576.
[45] X. Jing, Z. Pu, S. Zheng, F. Wang, H. Qi, Nanosecond laser induced microstructure features and effects thereof on the wettability in zirconia, Ceram. Int. 46 (2020) 24173–24182.
[46] Q. Li, H. Zhang, M. Gao, J. Li, H. Zhang, High-temperature wetting behavior of molten Ni-based superalloy on Y_2O_3 ceramics with different surface microstructures, J. Mater. Process. Technol. 294 (2021) 117094–117101.
[47] S.A. Egorov, K. Binder, When does Wenzel's extension of Young's equation for the contact angle of droplets apply? A density functional study, J. Chem. Phys. 152 (2020) 194707–194726.
[48] P. Chindaprasirt, P. Jitsangiam, P.K. Pachana, U. Rattanasak, Self-cleaning superhydrophobic fly ash geopolymer, Sci. Rep. 13 (2023) 44–52.
[49] F. Bohlooli, A. Anagri, S. Mori, Development of carbon-based metal free electrochemical sensor for hydrogen peroxide by surface modification of carbon nanowalls, Carbon 196 (2022) 327–336.
[50] Z.-Y. Zhang, T.-Y. Huang, D.-J. Zhai, H.-B. Wang, K.-Q. Feng, L. Xiang, Study on Zn-doped antibacterial bioactive coatings on Ti6Al4V titanium alloy surfaces by micro-arc oxidation, Surf. Coating. Technol. 467 (2023) 129724–129732.
[51] N. Tarasenka, V. Kornev, M. Rzheutski, E. Lutsenko, S. Chakrabarti, T. Velusamy, D. Mariotti, N. Tarasenko, Fabrication of luminescent silicon carbide nanoparticles by pulsed laser synthesis in liquid, Appl. Phys. A 128 (2022) 749–762.
[52] F.H. Rajab, Z. Liu, L. Li, Production of stable superhydrophilic surfaces on 316L steel by simultaneous laser texturing and SiO_2 deposition, Appl. Surf. Sci. 427 (2018) 1135–1145.